ACS OMEGA

Article

Cite This: ACS Omega 2017, 2, 7672-7681

http://pubs.acs.org/journal/acsodf

Bicontinuous Spider Network Architecture of Free-Standing $MnCoO_X$@NCNF Anode for Li-Ion Battery

Jitendra Shashikant Samdani, Tong-Hyun Kang, Chunfei Zhang, and Jong-Sung Yu*

Department of Energy Science and Engineering, Daegu Gyeongbuk Institute of Science and Technology (DGIST), Daegu 42988, Republic of Korea

Supporting Information

ABSTRACT: Herein, a smart strategy is proposed to tailor unique interwoven nanocable architecture consisting of $MnCoO_x$ nanoparticles embedded in one-dimensional (1D) mesoporous N-doped carbon nanofibers (NCNFs) by using electrospinning technique. The as-prepared network mat of N-doped carbon nanofibers with embedded $MnCoO_x$ nanoparticles ($MnCoO_x$@NCNFs) is tested as a current collector-free and binder-free flexible anode, which eliminates slurry preparation process during electrode fabrication in the Li-ion battery (LIB). The $MnCoO_x$@NCNFs possess versatile structural characteristics that can address simultaneously different issues such as poor conductivity, low cycling stability, volume variation, flexibility, and binder issue associate with the metal oxide. The free-standing mat electrode shows not only high initial discharge and charge capacities but also reversible discharge cycling stability of almost 80% retention up to 100 cycles and 60% retention up to 500 cycles at 1.0 A/g. Such high Li storage capacity and excellent cycling stability are attributed to the unique flexible and free-standing spider network-like architecture of the 1D $MnCoO_x$@NCNFs that provides the platform for bicontinuous electron/ion pathways for superior electrochemical performance. Along with excellent electrochemical performance, simple synthesis procedure of unique binder-free $MnCoO_x$@NCNFs can achieve cost-effective scalable mass production for practical use in a flexible mode, not merely in LIBs but also in a wide spectrum of energy storage fields.

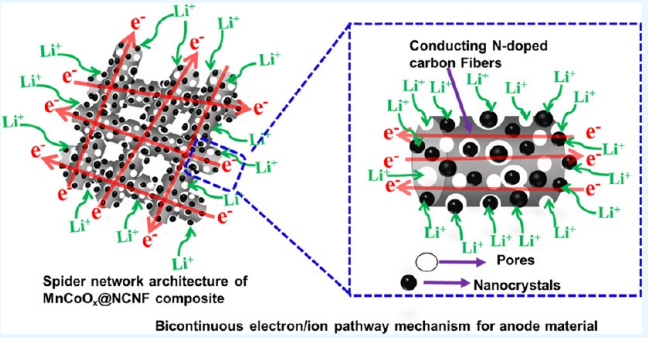

INTRODUCTION

In modern society, demand of portable electronic devices is rapidly increasing; hence, electrochemical storage devices attract great interest as power systems in the electronic market.[1−3] Lithium-ion battery (LIB) is the most promising candidate as an electrochemical storage device because of its high energy density and operating voltage.[4] Currently, graphite has been used as an anode material for the commercially available LIB, but it has some limitations such as low specific capacitance and energy density.[5] Therefore, immense efforts have been focused to develop new anode materials as alternatives to graphite for LIB.[6] Nowadays, single and binary transition metal oxides (TMOs)[7,8] and mixed transition metal oxides (MTMOs)[9,10] have attracted tremendous attention of research community, as they can store a large quantity of Li^+ (500−1000 mAh/g) via spatially varied conversion-type reaction mechanisms.[11] Among the TMOs, cobalt and manganese have been extensively used for energy storage because both of them show variable oxidation states.[12] Many researchers are currently working on engineering the micro/nanostructure of $MnCo_2O_4$ and mixed manganese cobalt oxides to overcome the volume change during Li^+ insertion/extraction. For instance, Li et al. fabricated a quasi-hollow microsphere structure of $MnCo_2O_4$ by tuning the synthesis strategy, which offered the large surface area and shortened the diffusion length of ion, to overcome the volume expansion during the charge/discharge.[13] Huang et al. developed a core−shell ellipsoidal $MnCo_2O_4$ structure, which showed the initial discharge capacity of 1433.3 mAh/g at 0.1 A/g.[14] Furthermore, a few more microstructures/nanostructures such as multicomponent assembled $MnCo_2O_4$ microspheres,[15] and hollow $MnCo_2O_4$ submicrospheres with multilevel interiors to help to buffer the volume variation of the anode material[16] have also been reported. However, these nanostructured $MnCo_2O_4$ materials suffer from poor electron transfer typical of oxide materials and, hence, need to combine with conductive carbonaceous materials to manage the electron transfer issue.

Chen et al. suggested that the graphene sheet was beneficial for the transportation of ions/electrons during battery operation in $MnCo_2O_4$/graphene sheet composite.[17] Likewise, Wang et al. demonstrated the synthesis of one-dimensional (1D) $CoMnO_x$/N-CNT composite by binding Mn−Co particles on nitrogen-doped carbon nanotubes (N-CNTs) through solvothermal method.[18] Moreover, Yun et al. synthesized $MnCo_2O_4$ microspheres with a uniform surface coating of conductive carbon layer to enhance the electro-

Received: August 22, 2017
Accepted: October 27, 2017
Published: November 8, 2017

DOI: 10.1021/acsomega.7b01228
ACS Omega 2017, 2, 7672−7681

chemical performance of $MnCo_2O_4$ microspheres.[19] However, these works need proper slurry preparation, which requires adequate combination of active material, binder, conductive additive, and solvent for optimization of the electrode in terms of specific capacity and cycle life in Li-ion battery, as illustrated by Kraytsberg et al.[20] Bhattacharjya et al. also demonstrated the effect of polymeric binder not only on the high specific capacity but also on the rate and cycling stability.[21] Currently, all of the commercial LIB electrodes utilize polymer binder. Although when used at an appropriate concentration in the electrode formulation, the binder is not that detrimental to the battery's energy density, the use of polymeric binder bothers the electrical conductivity of active material and its utility as an anode material in addition to extra cost for the binder in a LIB. To overcome the barrier of binder, Li et al. demonstrated the growth of one-dimensional $MnCo_2O_4$ nanowires on a nickel foam as a binder-free anode material for LIB, and Hou et al. reported a three-dimensional hierarchical $MnCo_2O_4$ nanosheet array on a carbon cloth.[22,23] Even though these types of electrode materials show good electrochemical performance, they still have the deficiency of simultaneous electron and ion conduction pathways and scalable mass production. Wei et al. illustrated the concept of simultaneous electron and ion conduction pathways for hierarchical lithium vanadium phosphate/carbon mesoporous nanowires, even though polymeric binder and conductive additives were used for the fabrication of coin cell.[24] Furthermore, Yang et al. used the lithium vanadium phosphate on the carbon nanofiber (CNF) as a high-performance cathode material.[25] Similarly, CNF,[26] MnO/CNF,[27] $FeCO_3$/CNF,[28] and Mn_3O_4-MnO/CNF[29] have also been studied as flexible anode materials for Li-ion batteries.

Herein, we report a first in situ synthesis of uniformly distributed $MnCoO_x$ nanoparticles encapsulated in a N-doped carbon nanofiber (NCNF) by using the electrospinning technique. In particular, a smart strategy is developed to fabricate a free-standing interwoven spider network architecture of unique one-dimensional (1D) NCNFs with embedded $MnCoO_x$ nanoparticles ($MnCoO_x$@NCNFs) and thus to enable binder-free and slurry preparation-free formulation process of the $MnCoO_x$@NCNF electrode. The $MnCoO_x$@NCNF electrode is found to effectively shorten Li^+ ion diffusion, relieve volume change, and provide effective electron conduction pathways during the lithiation/delithiation process of the metal oxide, which can greatly improve the electrochemical performance of the cell.

RESULTS AND DISCUSSION

The as-prepared composite contains $MnCoO_x$ nanoparticles embedded in mesoporous N-doped carbon nanofibers ($MnCoO_x$@NCNFs) by using the electrospinning technique. The steps involved in the material synthesis are shown in Figure 1a. At the initial stage, polyacrylonitrile (PAN)/dimethylformamide (DMF) solution along with metal precursors undergoes electrospinning process to get Mn−Co−PAN fiber composite. Further, the electrospun Mn−Co−PAN fiber is initially calcined at 250 °C for 1 h and then at rising temperature up to 700 °C for 1 h under N_2 flows. During the calcination process, acetate groups from Mn and Co convert into CO_2 and other gases, and PAN also decomposes to become carbon framework and produce NH_3. Because of the evolution of CO_2, NH_3, and other gases, mesosize pores were created on the carbon fiber backbone. Moreover, in the inert atmosphere, the cyclic structure of PAN polymer gets opened

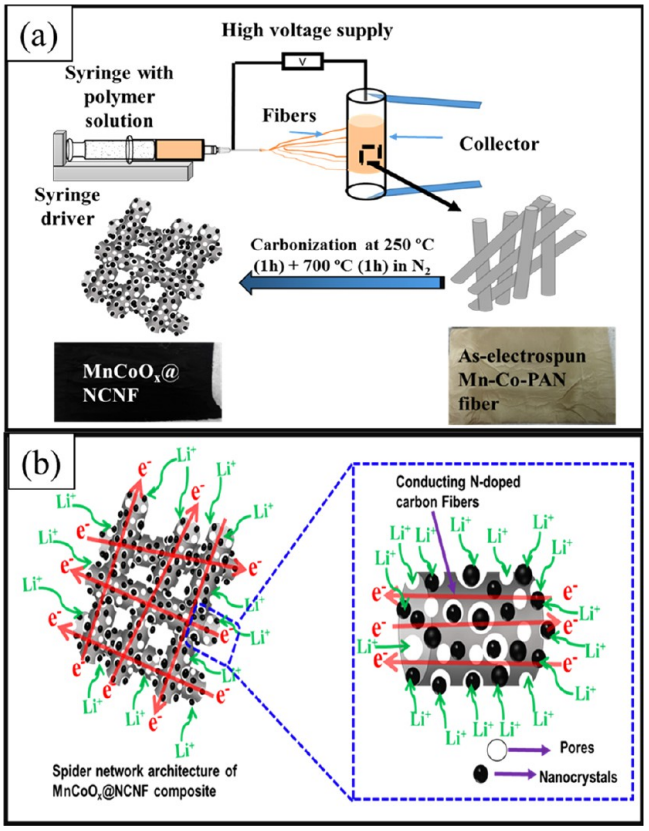

Figure 1. Schematic illustration of (a) preparation of $MnCoO_x$@NCNF composite by electrospinning and carbonization processes, and (b) interwoven spider network architecture of $MnCoO_x$@NCNF composite with bicontinuous electron/ion transport pathways.

and transformed into the carbon chain. These carbon chains further arranged themselves to form a graphitic carbon encapsulating the $MnCoO_x$ nanoparticles in the carbon fiber framework.[30] Metal oxide-free N-doped CNFs (NCNFs) were also synthesized in the same way as that of $MnCoO_x$@NCNF process without the addition of Mn-acetate and Co-acetate sources. Because there is no metal precursor, no visible pores are formed on the surface of NCNF. The as-prepared $MnCoO_x$@NCNF film mat as well as the NCNF film shows excellent flexibility, as shown in Movie S1 (Supporting Information), and hence can be directly used as a current collector/binder-free anode material in LIBs.

Thermogravimetric analysis (TGA) is carried out to confirm the exact amount of $MnCoO_x$ in the composite and indicates the presence of 66 wt % metal oxide, as shown in Figure S1 (Supporting Information). Therefore, the as-prepared interwoven spider network architecture of $MnCoO_x$@NCNFs possesses proper amount of $MnCoO_x$ and NCNF. The $MnCoO_x$@NCNF composite can address simultaneously different issues such as poor conductivity, low cycling stability, volume variation, and flexibility of the metal oxide, as well as troublesome binder issue. In addition, it provides unique bicontinuous electron/ion transport pathways for superior electrochemical performance, as illustrated in Figure 1b, which is attributed to the synergistic effect of $MnCoO_x$ nanoparticles and porous NCNFs. This will be considered more in the following discussion.

The X-ray diffraction (XRD) patterns of $MnCoO_x$@NCNF composite match well with the mix phases of $MnCo_2O_{4.5}$ and

DOI: 10.1021/acsomega.7b01228
ACS Omega 2017, 2, 7672−7681

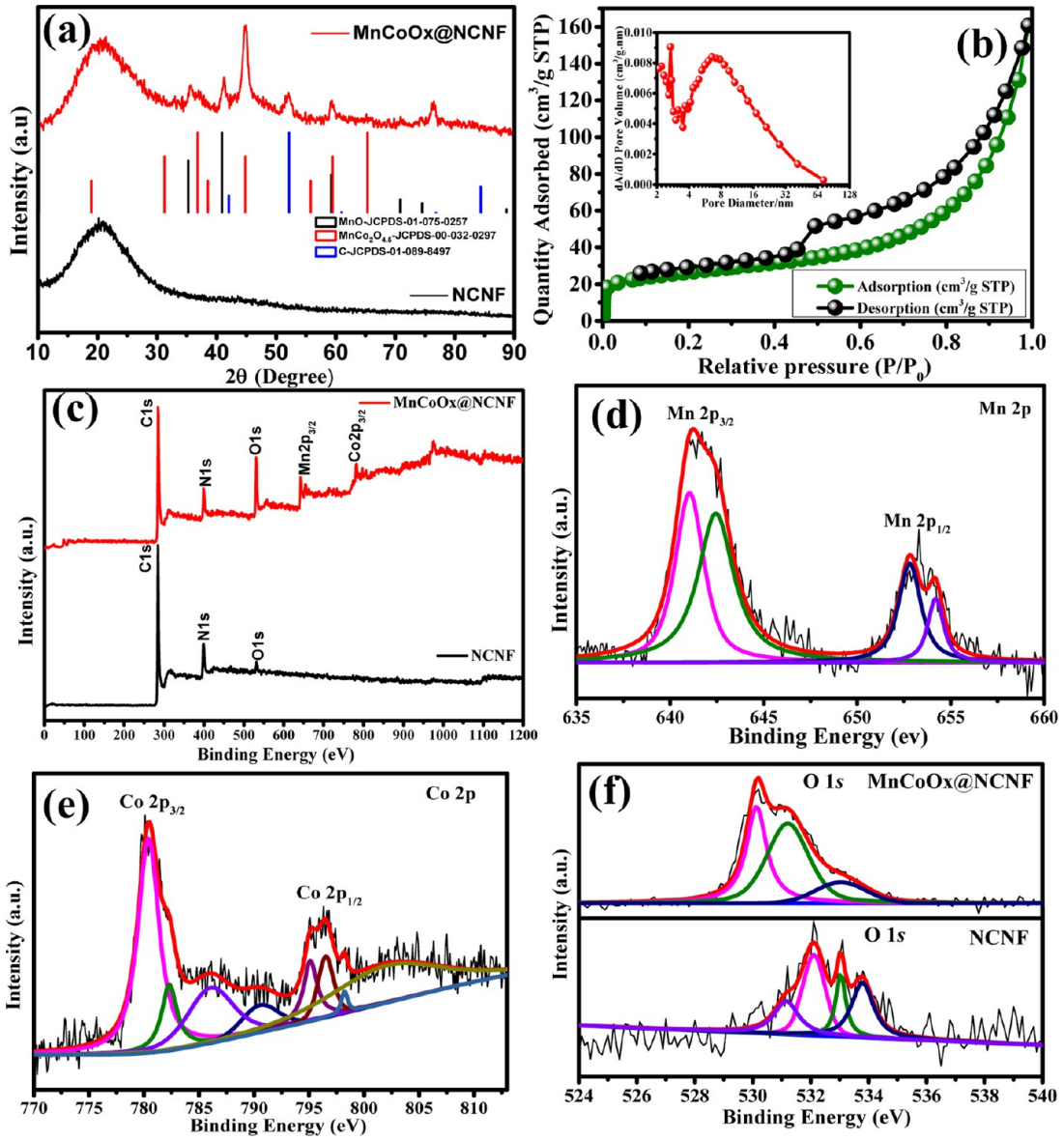

Figure 2. (a) XRD spectra of $MnCoO_x$@NCNF and NCNF samples, (b) N_2 adsorption isotherm of $MnCoO_x$@NCNFs, (c) X-ray photoelectron survey spectra of $MnCoO_x$@NCNF and NCNF samples, and deconvoluted X-ray photoelectron spectra of (d) Mn 2p, (e) Co 2p, and (f) O 1s for $MnCoO_x$@NCNF and NCNF samples.

MnO in accordance with JCPDS No. [00-032-0297] and [01-07-0257], respectively, as shown in Figure 2a. Because the $MnCoO_x$@NCNF composite shows the mixture phase peaks of MnO and $MnCo_2O_{4.5}$, all of the peaks of MnO and $MnCo_2O_{4.5}$ may not be observable in the XRD spectrum due to their low crystallinity and co-interference. A broad peak at 20° in both the $MnCoO_x$@NCNF and NCNF materials is ascribed to the graphitic carbon. The nitrogen adsorption−desorption study of $MnCoO_x$@NCNFs reveals the type II/IV isotherms in Figure 2b. The specific surface area (SSA) of $MnCoO_x$@NCNFs is observed to be 94 m^2/g, whereas NCNFs show a low SSA of 9.0 m^2/g, with no obvious isotherm type. As shown in the inset of Figure 2b, the as-prepared $MnCoO_x$@NCNF material shows two kinds of mesopores (with maximum at 3 and 9 nm), which can assist in the fast diffusion of Li ions.

Furthermore, X-ray photoelectron spectroscopy (XPS) analysis was also carried out to understand the valance states of Mn and Co in the $MnCoO_x$@NCNFs. The survey spectrum of the pure NCNFs shows the C, N, and O peaks, whereas the $MnCoO_x$@NCNF composite clearly points out the presence of additional peaks of Mn and Co in Figure 2c. By using a Gaussian fitting method, Mn 2p spectrum features two main spin−orbit lines of Mn $2p_{3/2}$ at 641.01 and Mn $2p_{1/2}$ at 652.77 eV with separation of 11.76 eV (Figure 2d). After precise fitting, the spectrum is deconvoluted into peaks at 641.01 and 652.77 eV, which correspond to the existence of Mn(II) and peaks at 642.46 and 654.40 eV, the characteristic peaks of Mn(III) cation.[31] The Co 2p X-ray photoelectron spectrum of $MnCoO_x$@NCNFs also demonstrates two characteristics peaks at 780.5 and 796.6 eV, corresponding to the Co $2p_{3/2}$ and Co $2p_{1/2}$ spin−orbit peaks, whereas prominent satellite peaks at 786.2 and 802.8 eV in the Co 2p spectrum confirm the co-presence of Co^{2+} and Co^{3+} (Figure 2e).[32] The deconvoluted O 1s spectrum in Figure 2f exhibits the photoelectron peaks at 530.11 eV, which certify the metal−oxygen bond and the presence of oxygen in the spinel structure lattice. In particular,

DOI: 10.1021/acsomega.7b01228
ACS Omega 2017, 2, 7672−7681

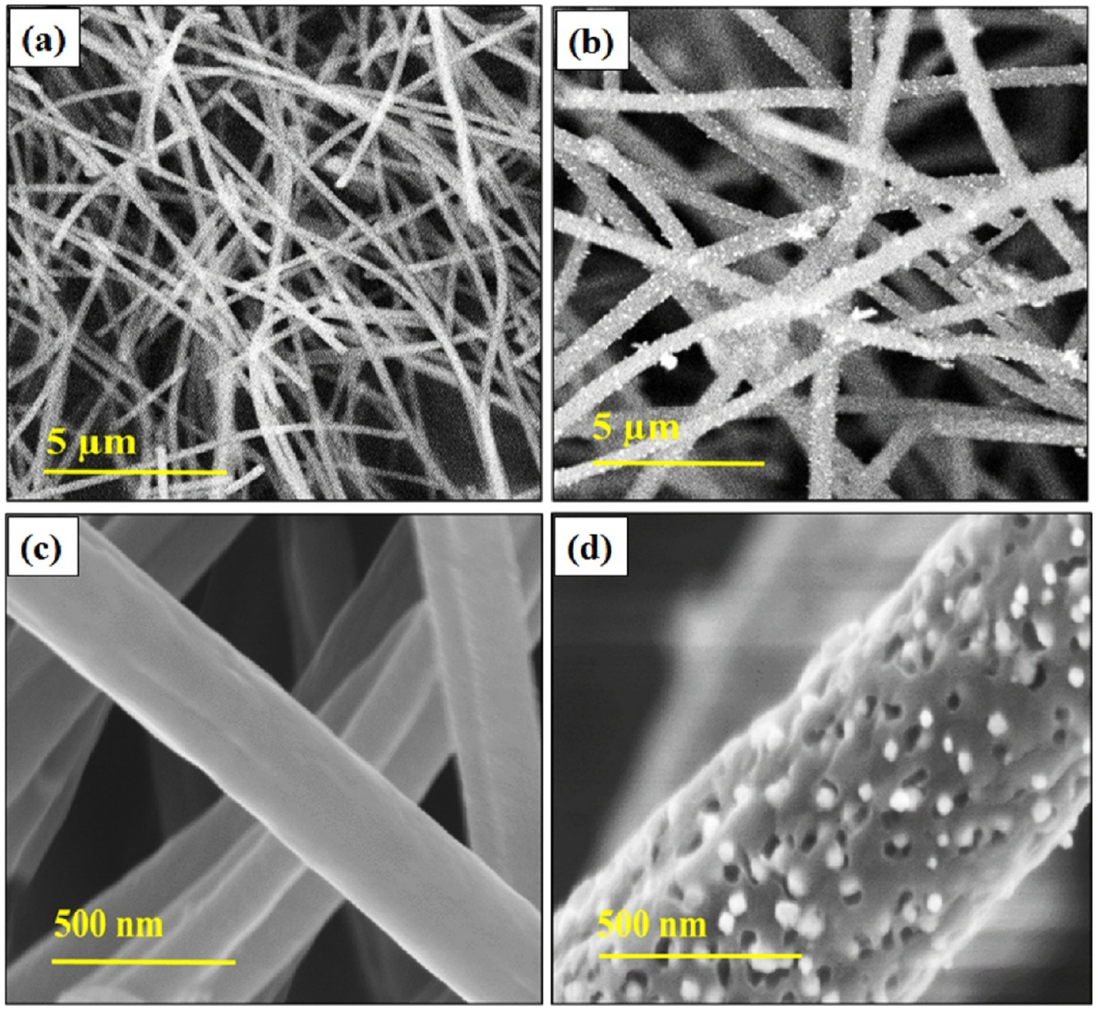

Figure 3. SEM images of (a, c) pristine NCNFs and (b, d) $MnCoO_x$@NCNFs at lower and higher magnifications, respectively.

additional peaks at 531.18 and 533.07 eV are ascribed to organic C−O and C═O.[33] Meanwhile, the O 1s peaks for metal oxide-free NCNF are deconvoluted into four peaks 531.16, 532.1, 533.1, and 533.8 eV. Furthermore, C 1s and N 1s X-ray photoelectron spectra of $MnCoO_x$@NCNF and NCNF samples are shown in Figure S2 (Supporting Information).

The morphology and microstructure of the as-prepared NCNFs and $MnCoO_x$@NCNFs show the interwoven nanocable architecture, as seen in Figure 3a,b. Figure 3a,c clearly shows the formation of fiber with uniform diameter and smooth surface of pristine NCNF without any visible pores on its surface, in accordance with its low surface area. On the other hand, Figure 3b,d shows the nanoparticles (less than 30 nm) of $MnCoO_x$ consistently embedded in the NCNF, as well as the mesopores with ∼25 nm in size on the backbone of the NCNF of $MnCoO_x$@NCNFs, which can be attributed to the evolution of CO_2, NH_3, and other gases during the carbonization of as-electrospun Mn−Co−PAN fibers (Figure 3d). Transmission electron microscopy (TEM) images of the metal oxide-free NCNFs in Figure 4a also justify the smooth surface without any visible pores and nanoparticles, whereas $MnCoO_x$@NCNFs shown in Figure 4b authenticate the presence of $MnCoO_x$ nanoparticles, which are homogeneously embedded in the NCNFs, in accordance with the scanning electron microscopy (SEM) images in Figure 3. In particular, it is enthralling to notice that in Figures 3 and 4a,b, the diameter (∼700 nm in size) of $MnCoO_x$@NCNF is much bigger than that of pure NCNFs (∼300−350 nm in size), although both were prepared in identical electrospinning conditions. The larger diameter of $MnCoO_x$@NCNF may be ascribed to the embedded $MnCoO_x$ nanoparticles and pores developed in the NCNF framework. In addition, the high-resolution TEM (HRTEM) images (Figure 4c,d) clearly exhibit the ubiquitous dispersion of $MnCoO_x$ particles and the formation of graphitic carbon layers in the $MnCoO_x$@NCNFs, which are beneficial for the conduction of electron/ion during the electrochemical study. Moreover, elemental mapping shown in Figure S3 (Supporting Information) confirms the uniform distribution of Mn, Co, C, N, and O in the as-prepared $MnCoO_x$@NCNF.

Slurry preparation needs extra works including troublesome polymeric binder during electrode fabrication, which restricts the kinetics of ions, electron transport, and long-term cycling/retention stability of electrode material and hence becomes a cause of deterioration in the LIB performance.

In this work, the as-prepared unique spider network mats of $MnCoO_x$@NCNFs and NCNFs were investigated as free-standing anode materials in a Li-ion half-cell, which eliminate slurry preparation process during electrode fabrication in LIB. To investigate the redox properties of the as-prepared $MnCoO_x$@NCNF and NCNF mat electrodes, cyclic voltammetry (CV) curves were measured between 0.01 and 3.00 V at a scan rate of 0.1 mV/s. The representative CV curves of the

DOI: 10.1021/acsomega.7b01228
ACS Omega 2017, 2, 7672−7681

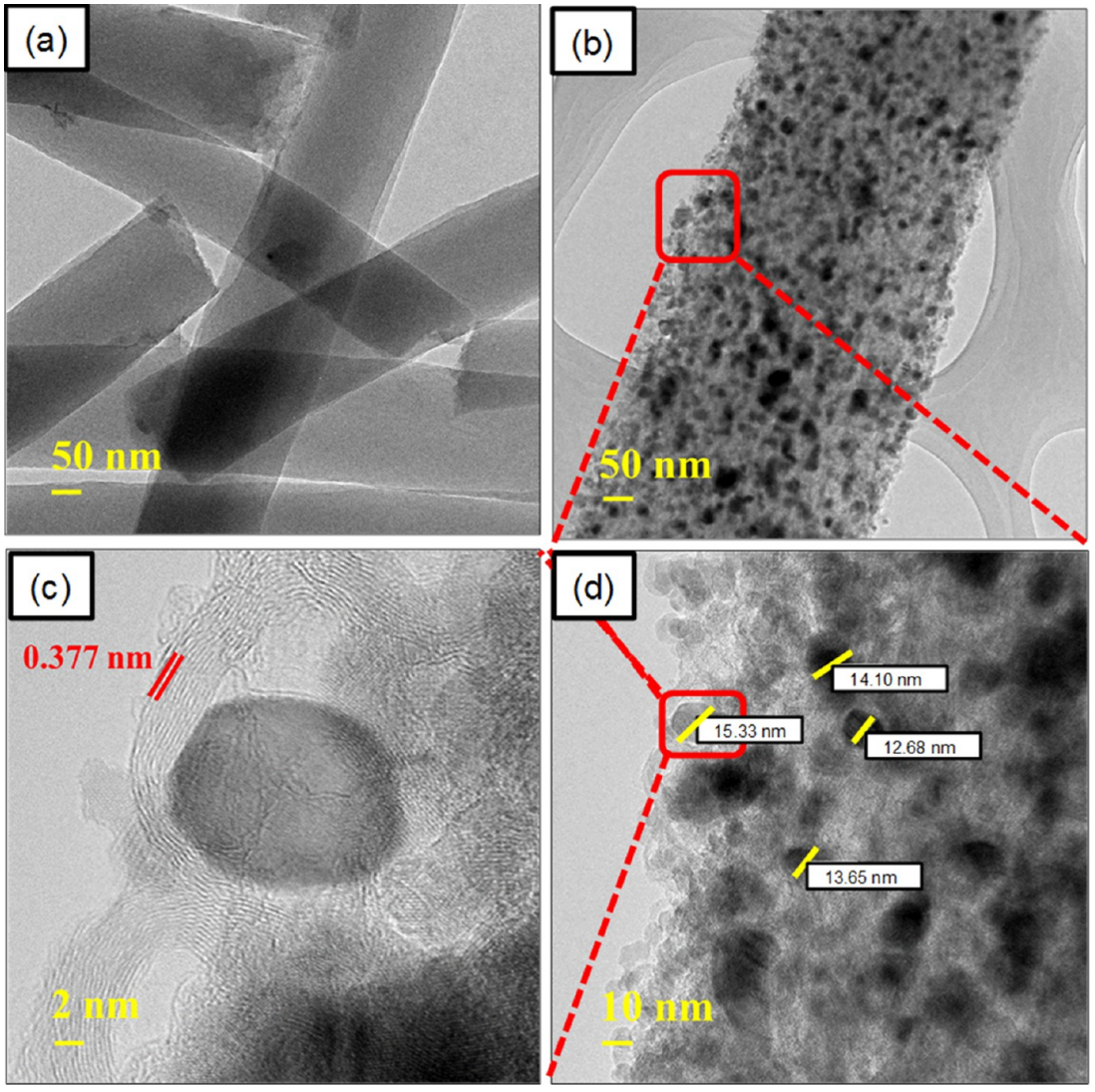

Figure 4. (a, b) TEM images of NCNF and $MnCoO_x$@NCNF samples, respectively, and (c, d) HRTEM images of $MnCoO_x$@NCNF at different magnifications.

binder-free $MnCoO_x$@NCNF electrode during the first five cycles are shown in Figure 5a. It is observed that during the first cycle, three reduction peaks can be identified in the cathodic sweep. A broad peak centered at 0.97 V corresponds to the initial reduction of Mn^{2+} to Mn^{1+} and $Co^{3.5+}$ to $Co^{1.5+}$.[34] The proposed reaction mechanism for the reduction of Mn and Co is shown as follows (eq 1).

$$MnCo_2O_{4.5} + 5Li^+ + 5e^- \rightarrow MnO_{0.5} + 2CoO_{0.75} + 2.5Li_2O \quad (1)$$

The other two reduction peaks at 0.66 and 0.53 V (Figure 5a) are associated with the reversible reactions between Li, $MnO_{0.5}$, and $CoO_{0.75}$ species, as seen in eqs 3 and 4.

$$MnO + 2Li^+ + 2e^- \rightarrow Mn + Li_2O \quad (2)$$

$$MnO_{0.5} + 1Li^+ + 1e^- \leftrightarrow \frac{1}{2}Li_2O + Mn \quad (3)$$

$$2CoO_{0.75} + 3Li^+ + 3e^- \leftrightarrow \frac{3}{2}Li_2O + 2Co \quad (4)$$

Besides, another extra sharp cathodic peak is obtained at 0.16 V, which corresponds to the complete irreversible reduction reaction (eq 2) of Mn^{2+} to Mn^0 and the formation of a solid electrolyte interphase (SEI) layer.[35,36] This may also prove the presence of the extra MnO crystal along with the $MnCo_2O_{4.5}$ in the as-synthesized $MnCoO_x$@NCNF material, as shown in the XRD signal in Figure 2a. In the anodic sweep, two broad peaks were observed at 1.29 and 2.05 V (vs Li/Li^+), which are assigned to the reoxidation of Mn^0 to Mn^{1+} and Co^0 to $Co^{1.5+}$, respectively, as seen in eqs 3 and 4. Later, from the second cycle onward, two pairs of redox couples at 0.33/1.29 V and 0.47/2.05 V are observed with stable peak positions, suggesting that the highly reversible conversion reactions start to dominate the Li^+ storage process.

To pursue eqs 1−4, ex situ XRD measurements were performed for charging and discharging tests at different voltages of $MnCoO_x$@NCNF coin cell in Figure S4 (Supporting Information). Small XRD peaks corresponding to MnO, CoO, and Li_2O, as well as metallic Mn and Co, were observed for the respective potentials, confirming the interaction of Li^+ ion with $MnCoO_x$ particles in $MnCoO_x$@NCNF electrode. In the case of NCNF electrode, a strong peak

DOI: 10.1021/acsomega.7b01228
ACS Omega 2017, 2, 7672−7681

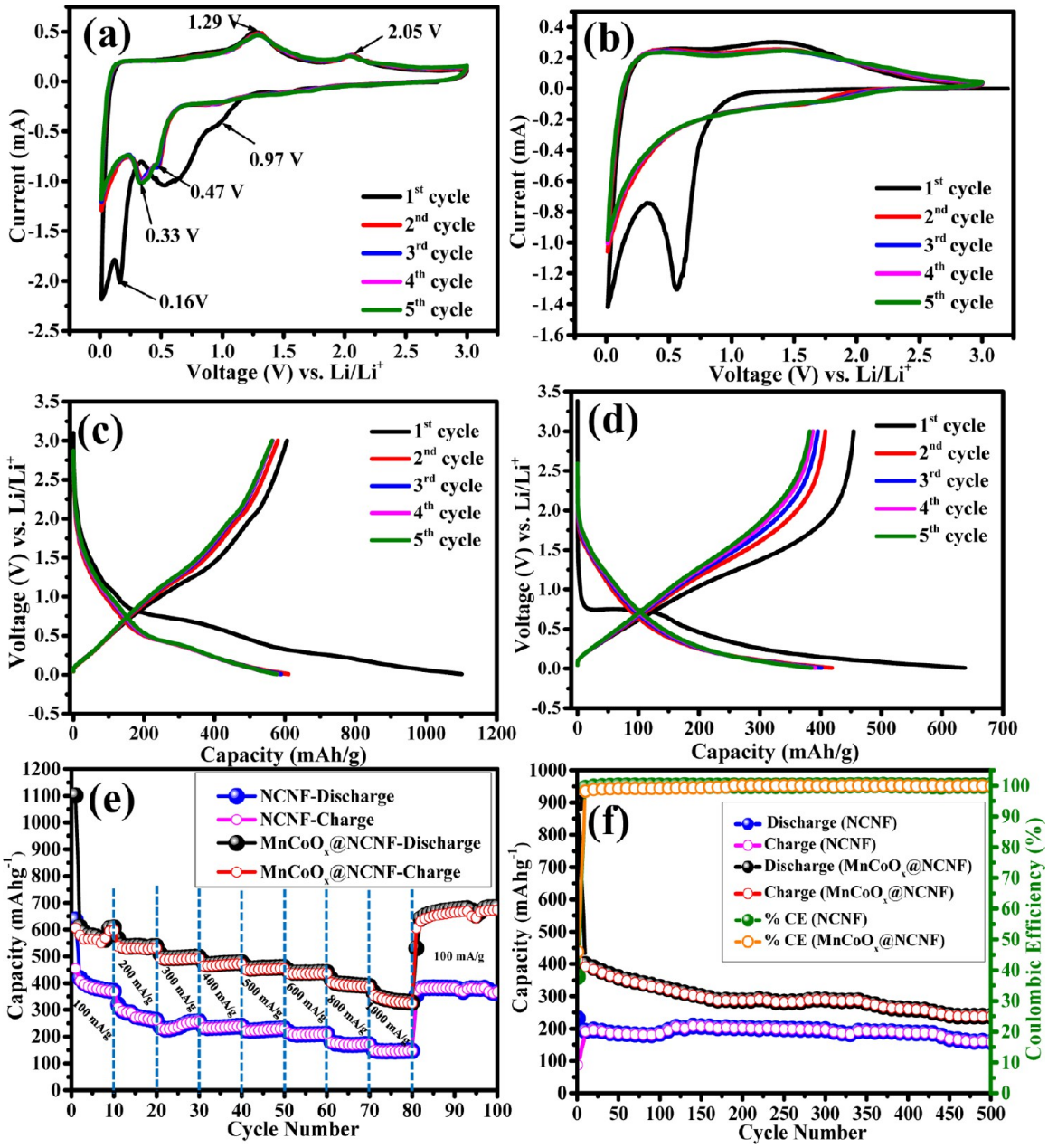

Figure 5. Electrochemical performance: (a, b) CV curves, (c, d) voltage−capacity curves at a current density of 100 mA/g for the first five cycles of $MnCoO_x$@NCNF and NCNF mat electrodes, respectively, (e) rate capability at different current densities, and (f) cyclic stability at a current density of 1.0 A/g of $MnCoO_x$@NCNF and NCNF mat electrodes, respectively.

at 0.56 V is observed in the first cycle and vanishes in the second cycle, as illustrated in Figure 5b, indicating the formation of the SEI film on the surface of NCNFs.[37,38] The discharge−charge characteristic curves of the $MnCoO_x$@NCNF electrode at a current density of 100 mA/g in the potential range of 0.01−3.00 V (vs Li^+/Li) are shown in Figure 5c. The discharge and charge capacities of the electrode material in first cycle were found to be 1103 and 610 mAh/g. The irreversible loss of capacity is attributed to the formation of protecting SEI film during the first discharge step. In the subsequent discharge/charge curves, reversible discharge/charge capacities acquired are 608 and 597 mAh/g, respectively, with a stable electrochemical behavior of the $MnCoO_x$@NCNF electrode. On the other hand, the NCNF electrode in Figure 5d shows the initial discharge and charge capacities of 637 mAh/g and 455 mAh/g, respectively, clearly indicating that the reversible discharge and charge capacities observed for $MnCoO_x$@NCNFs are higher than those for NCNFs.

Areal and volumetric capacities are also critical for practical battery applications and were measured with loading amount and density of the electrode materials. Discharge and charge areal capacities of the first five cycles of $MnCoO_x$@NCNF and NCNF mat electrodes were calculated and shown in Figure S5 (Supporting Information). To examine the volumetric capacity of the as-prepared $MnCoO_x$@NCNF and NCNF electrodes, the thickness of the electrode was measured before coin cell assembly by the cross-sectional SEM images shown in Figure S6 (Supporting Information), and related calculation is also shown in the Supporting Information. The areal and volumetric capacities determined for the first cycle were calculated to be

DOI: 10.1021/acsomega.7b01228
ACS Omega 2017, 2, 7672−7681

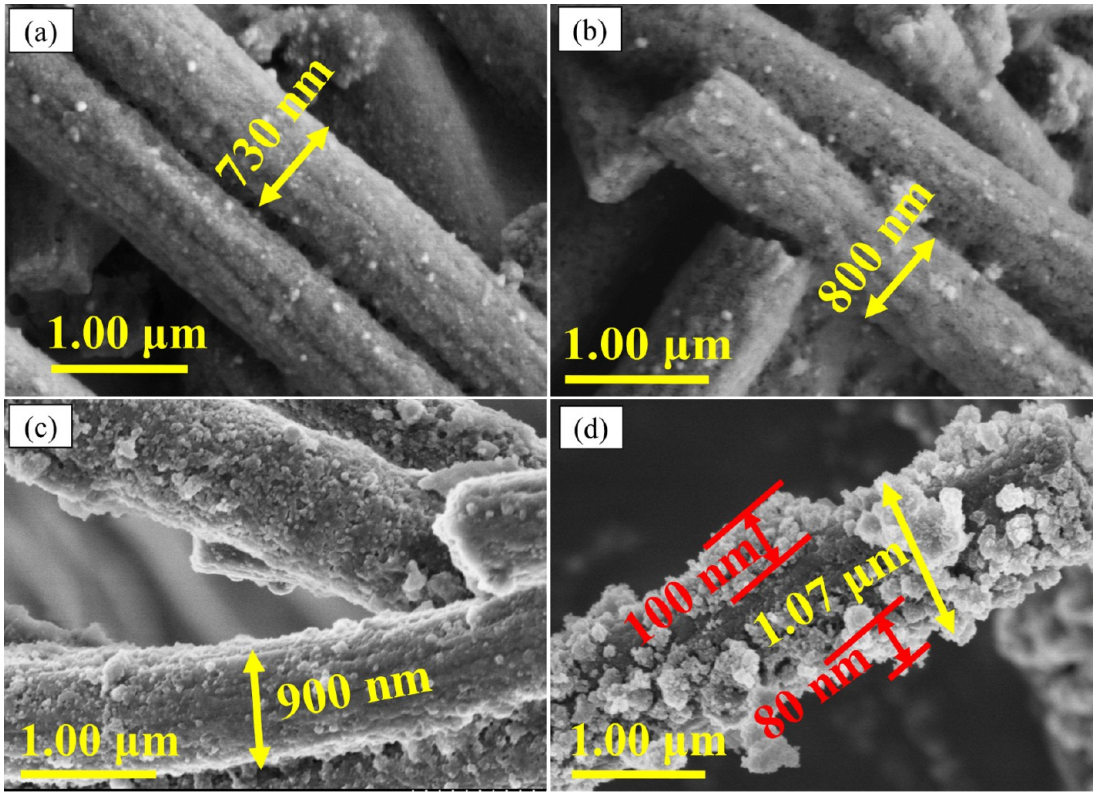

Figure 6. SEM images after (a) 1, (b) 10, (c) 100, and (d) 500 cycling performance tests of $MnCoO_x$@NCNF electrode at 1.0 A/g.

3.96 mAh/cm^2 and 162.2 mAh/cm^3 for discharge and 2.18 mAh/cm^2 and 89.7 mAh/cm^3 for charge, respectively, for $MnCoO_x$@NCNF electrode. By comparison, the corresponding areal and volumetric capacities for the first cycle of the pure NCNF electrode were determined to be 1.40 mAh/cm^2 and 61.18 mAh/cm^3 for discharge and 1.00 mAh/cm^2 and 43.7 mAh/cm^3 for charge, respectively. These results further support the results for specific capacities in Figure 5 and clearly demonstrate the importance of the active $MnCoO_x$ nanoparticles for enhanced electrochemical performance in $MnCoO_x$@NCNF electrode.

Additionally, Figure 5e represents the rate capability of each of $MnCoO_x$@NCNF and NCNF electrodes. Initially, $MnCoO_x$@NCNF electrode was cycled at 100 mA/g. The capacity was stabilized at 609 mAh/g after 10 cycles, which is already almost 2 times higher than that of the metal oxide-free NCNF electrode. Then, the current density for $MnCoO_x$@NCNF electrode was stepwise increased to 200, 300, 400, 500, 600, 800, and 1000 mA/g, and the average discharge capacities of 537, 495, 475, 455, 440, 390, and 335 mAh/g, respectively, were obtained after 10 cycles at each of these current densities. Interestingly, when the current density finally returns to its original value of 100 mA/g after 80 cycles, the capacity is returned and further increased to 680 mAh/g. This exceptionally high rate capability is due to the presence of $MnCoO_x$ nanoparticles embedded into the NCNF framework and the free-standing spider network architecture mat of 1D $MnCoO_x$@NCNF nanocables. This unique free-standing spider network mat structure facilitates the movement of electrons generated from the conversion-type reaction between $MnCoO_x$ and Li^+. In addition, the mesosize pores on the $MnCoO_x$@NCNF backbone allocate the platform for a fast diffusion of Li^+ ion during discharge/charge. The rate capability of NCNF electrode follows the same trends as that of $MnCoO_x$@NCNF electrode, but the capacity values are much less, which confirms that the ubiquity of $MnCoO_x$ nanoparticles and mesopores helps to enhance the capacity of $MnCoO_x$@NCNF electrode.

Furthermore, the Li^+ diffusion constant was calculated for $MnCoO_x$@NCNF anode material by Randles Sevchik in eq 5.[39] For the Li^+ ion diffusion coefficient, cyclic voltammograms of variation scan rates were performed for $MnCoO_x$@NCNF electrode (Figure S7a, Supporting Information).

$$I_p = 2.69 \times 10^5 n^{3/2} S\, C_0 D^{1/2} \vartheta^{1/2} \quad (5)$$

where I_p is the peak current, n is the number of electrons, S is the active surface area of the electrode, C_0 is the concentration of Li ion, D is the diffusion coefficient, and ϑ is the scan rate. From the slope of linear fitting line for peak intensity of A (see Figure S7b, Supporting Information), the diffusion coefficients of $MnCoO_x$@NCNF were determined to be 1.008×10^{-6} and 2.7×10^{-6} cm^2/s for oxidative and reductive peak currents, respectively.

To examine the practical application of electrode, the cyclic stability of each of $MnCoO_x$@NCNF and NCNF electrodes was performed at the current density of 1.0 A/g for 500 cycles, as shown in Figure 5f. The $MnCoO_x$@NCNF electrode shows the initial discharging capacity of 898 mAh/g and the second discharge capacity of 428 mAh/g at 1.0 A/g, which corresponds to 52% loss in the initial capacity. From the second cycle onward, the discharging capacity shows an almost 80% retention for 100 cycles and 60% retention for 500 cycles (Figure 5f).

To investigate the volume expansion of the as-prepared $MnCoO_x$@NCNFs during cycling test, scanning electron microscopy (SEM) was employed after different number of

DOI: 10.1021/acsomega.7b01228
ACS Omega 2017, 2, 7672−7681

cycles. It is clearly observed that very thin layer was deposited on the surface of the NCNFs after 1 and 10 cycles (Figure 6a,b) compared to the initial diameter (~700 nm) of the $MnCoO_x$@NCNFs before cycling. The diameter increases to ~800 nm after 10 cycles, which corresponds to 100 nm increment compared to that before cycling. When the cycle number increases further from 10 to 100−500 cycles (Figure 6c,d), the diameter of the $MnCoO_x$@NCNFs also increased to ~1000 nm, which may be ascribed to the volume expansion of $MnCoO_x$ particles and the formation of thick layer of SEI film. Interestingly, 50−100 nm thick layer of particle-like aggregation over the NCNFs is observed and can be attributed to the formation of SEI film. By comparison, similar type of layer formation also occurs on the metal oxide-free NCNFs after different number of cycles at 1.0 A/g, as shown in Figure S8, Supporting Information.

Electrochemical activity of the present nanostructured $MnCoO_x$@NCNF electrode was accessed by comparing with other similar Mn−Co metal oxide electrodes as presented in Table S1 (Supporting Information). Although it is not possible to make a fair comparison due to different experimental conditions, in general, the current $MnCoO_x$@NCNF network demonstrates a higher capacity and a more stable cycle and rate capability in addition to a much simpler electrode design with no current collector and binder. It is attributed to the unique spider network architecture of $MnCoO_x$@NCNFs and mesopores on the backbone of the fiber.

To further clarify the electrochemical performance of the as-prepared materials, alternating current impedance measurements (Figure S9, Supporting Information) were performed on the $MnCoO_x$@NCNF and NCNF electrodes. The Nyquist plots were obtained in freshly prepared coin cell in the frequency range from 100 kHz to 10 mHz. The intercept on the Z real axis in the high-frequency region represents the resistance of electrolyte (R_s) and the diameter of the semicircle indicates the charge transfer resistance (R_{ct}), relating to the charge transfer through the active materials and electrolyte.[40] The vertical line in the low-frequency region indicates Warburg impedance (Z_W), which is related to the diffusion of Li^+ in the electrode.[41,42] The diameter of the semicircle for $MnCoO_x$@NCNF electrode is smaller than that of the NCNF electrode, suggesting the charge transfer is faster for the former probably because of the presence of mesopores and $MnCoO_x$ nanoparticles on the $MnCoO_x$@NCNF electrode.[43−45]

Bicontinuous electron/ion transport pathway mechanism is proposed as shown in Figure 1b. As a proof of the concept, the as-prepared $MnCoO_x$@NCNF composite shows superior anode electrochemical properties compared to pristine $MnCoO_x$-free NCNF electrode. It is because $MnCoO_x$ crystals in the $MnCoO_x$@NCNF composite enhance the interaction with Li^+ ion and follow the conversion-type reactions as illustrated in eqs 1−4. During the conversion reactions, the generated electrons are easily transported through the 1D conducting NCNF scaffold, and the presence of mesopores on the surface provides effective pathways for rapid Li^+ ion diffusion. Thus, this bicontinuous electron/ion pathway mechanism is achievable as a result of unique free-standing spider network architecture of $MnCoO_x$@NCNFs and found to be in good agreement with their superior electrochemical performance.

CONCLUSIONS

In conclusion, this current work is considered to clearly demonstrate the following key points.

1. $MnCoO_x$ particles are in situ encapsulated in mesoporous N-doped carbon nanofiber without disturbing the flexibility of the NCNFs.
2. As-prepared flexible interwoven nanocable architecture of 1D $MnCoO_x$@NCNFs is tested as a free-standing current collector/binder-free anode material for Li-ion battery, which can eliminate slurry preparation process during electrode fabrication in LIB.
3. For conversion-type lithiation/delithiation processes, the unique binder-free $MnCoO_x$@NCNFs boast of excellent level of cyclic stability with high specific capacity.
4. The unique spider network architecture of $MnCoO_x$@NCNFs assists to effectively shorten Li+ ion diffusion, provide effective electron conduction pathways, and buffer the volume variation during lithiation/delithiation processes.
5. The as-prepared unique $MnCoO_x$@NCNF network pursues the bicontinuous electron/ion pathway mechanism, enabling enhanced electrochemical performance.
6. Synthesis process of $MnCoO_x$@NCNFs is very simple and cost-effective, along with scalable production for practical use in flexible mode, not merely in LIBs but also in a wide spectrum of energy storage fields.

Therefore, the as-prepared $MnCoO_x$@NCNF network was able to address simultaneously several different kinds of issues such as poor conductivity, low cycling stability, flexibility, volume variation of the metal oxides, and slurry preparation during electrode formulation. The bicontinuous electron/ion transport pathway mechanism will promote further academic research, whereas the scalable production of flexible interwoven architectures of unique $MnCoO_x$@NCNFs will gain spotlight in the industry. This type of free-standing $MnCoO_x$@NCNF network will pave a new direction in the fabrication of current collector/binder-free flexible electrodes in battery and supercapacitor.

EXPERIMENTAL SECTION

Raw Materials. Polyacrylonitrile (PAN, MW 150 000), manganese acetate dihydrate ($Mn(Ac_2)\cdot 2H_2O$), and cobalt acetate tetra hydrate ($Co(Ac_2)\cdot 4H_2O$) were purchased from Sigma-Aldrich. *N*,*N*-Dimethylformamide (DMF) was procured from Alfa Aesar.

Synthesis of $MnCoO_x$@NCNFs and NCNFs. Polyacrylonitrile (PAN, 1g, MW 150 000) was dissolved in 10 mL of *N*,*N*-dimethylformamide (DMF) at 70 °C and stirred for 4 h. $Mn(Ac_2)\cdot 2H_2O$ (2 mmol) and $Co(Ac)_2\cdot 4H_2O$ (4 mmol) were mixed together, and the mixture was added slowly to the as-prepared PAN solution with vigorous mechanical stirring at 70 °C. The whole mixture was then stirred for another 4 h to get the precursor solution for electrospun. The precursor solution was loaded into a plastic syringe equipped with 23 gauge stainless needle. The 8 mL of solution was electrospun onto a drum collector covered with aluminum foil. The distance between the tip and the collector was kept constant at 18 cm, and the rotation of the drum was maintained at 500 rpm during the electrospinning process. The electrospinning process was carried out at an applied voltage of 16 kV, with a feeding speed of 1 mL/h. The electrospun Mn−Co−PAN fiber film was peel off from Al foil and further stabilized and carbonized according

DOI: 10.1021/acsomega.7b01228
ACS Omega 2017, 2, 7672−7681

to programmed processes at 250 and 700 °C in N_2 atmosphere to get $MnCoO_x$ nanoparticles embedded into the N-doped porous CNFs ($MnCoO_x$@NCNFs).

Material Characterization. Structural property of the as-prepared materials was examined by X-ray diffraction (XRD) using Rigaku Smartlab and PANalytical diffractometer. The spectra were recorded at a scan rate of 3°/min with a Cu Kα target (λ = 0.15406 nm) using a Ni β-filter operating at voltages of 40 and 45 kV and tube currents of 15 and 40 mA. Scanning electron microscopy (SEM), transmission electron microscopy (TEM), and high-resolution TEM (HRTEM) images were recorded to obtain the information on the surface morphologies of the as-prepared materials. The SEM images were obtained using a Hitachi S-4700 microscope operated at an acceleration voltage of 10 kV. TEM and HRTEM images were collected on HF-3300 (Hitachi Ltd., Japan) microscope operated at an acceleration voltage of 300 kV at the center for core research facility (CCRF) in DGIST. Elemental mappings were performed on a scanning transmission electron microscope (STEM) operated at 300 kV. X-ray photoelectron spectroscopy (XPS) analyses were carried out with AXIS−NOVA (Kratos) X-ray photoelectron spectrometer using monochromator Al Kα X-ray source ($h\upsilon$ = 1486.6 eV) operated at 150 W under base pressure of 2.6×10^{-9} Torr. The nitrogen adsorption−desorption isotherms were measured at −196 °C using a Micromeritics ASAP 2020 system. Specific surface areas of the samples were determined by nitrogen adsorption data in the relative pressure range from 0.05 to 0.2 using the Brunauer−Emmett−Teller (BET) equation. Total pore volume was determined from the amount of gas adsorbed at the relative pressure of 0.99.

Electrochemical Characterization. The electrochemical measurements of the as-prepared $MnCoO_x$@NCNF and NCNF mat electrodes were executed through CR2032 coin-type test cell (Hohsen Corporation, Japan). In coin cell fabrication, Li metal foil (99.9% purity and 150 μm thickness), 1.0 M $LiPF_6$ in ethylene carbonate/dimethyl carbonate (1:1 in volume), and microporous polypropylene sheet (Celgard, 2400) were used as counter/reference electrode, electrolyte, and separator, respectively. The as-prepared $MnCoO_x$@NCNF and NCNF mat materials were punched into a circular shape with 14 mm diameter, and the circular-shaped material can be directly used as the anode without using a current collector and adding any conductive agent or binder materials, i.e., as a free-standing anode material. The punched $MnCoO_x$@NCNF and NCNF circular materials with 14 mm diameter possess areal loadings of about 3.5−3.6 mg/cm^2 and 2.2−2.3 mg/cm^2, respectively. To remove moisture, the as-prepared materials were dried in a vacuum oven at 60 °C overnight. The vacuum-dried material was assembled into a CR2032 coin-type cell in an argon-filled glovebox. The cyclic voltammetry (CV) curves of the cells were recorded on a biologic electrochemical workstation (Biologic VSP). All of the CVs were carried out with a scan rate of 0.1 mV/s, over the potential range of 0.01−3.00 V. On the other hand, the charge−discharge behaviors of the cells were characterized by BaSyTech multichannel battery test system at room temperature at various current densities between the potential range of 0.01 and 3.00 V.

■ ASSOCIATED CONTENT

Supporting Information

The Supporting Information is available free of charge on the ACS Publications website at DOI: 10.1021/acsomega.7b01228.

TGA, XPS, elemental mapping, ex situ XRD measurement of $MnCoO_x$@NCNF composite, voltage−areal capacity curves, cross-sectional SEM images, volumetric capacity calculations, scan rate variation cyclic voltammograms, SEM images after cycling, and electrochemical impedance spectroscopy of $MnCoO_x$@NCNF and NCNF electrodes (PDF)

Demonstration of excellent flexibility of as-prepared $MnCoO_x$@NCNF film, which hence can be directly used as a free-standing and current collector/binder-free anode material in LIBs (MPG)

■ AUTHOR INFORMATION

Corresponding Author

*E-mail: jsyu@dgist.ac.kr. Tel: +82-53-785-6443. Fax: +82-53-785-6409.

ORCID

Jong-Sung Yu: 0000-0002-8805-012X

Notes

The authors declare no competing financial interest.

■ ACKNOWLEDGMENTS

We gratefully acknowledge financial support by Global Frontier R&D program on Center for Multiscale Energy System (NRF 2011-0031571) and NRF Grant (NRF 2014K2A3A1000240) funded by the Ministry of Education, Science and Technology of Korea. We also thank Byong-June Lee and Jong-Deok Park for helping in BET and TEM measurements. Special thanks is given to the CCRF at DGIST and KBSI at Daegu and Pusan for SEM, TEM, and XPS measurements.

■ REFERENCES

(1) Armand, M.; Tarascon, J. M. Building better batteries. *Nature* **2008**, *451*, 652−657.

(2) Tarascon, J. M.; Armand, M. Issues and challenges facing rechargeable lithium batteries. *Nature* **2001**, *414*, 359−367.

(3) Chen, Y. M.; Yu, X. Y.; Li, Z.; Paik, U.; Lou, X. W. D. Hierarchical MoS_2 tubular structures internally wired by carbon nanotubes as a highly stable anode material for lithium-ion batteries. *Sci. Adv.* **2016**, *2*, No. e1600021.

(4) Kang, B.; Ceder, G. Battery materials for ultrafast charging and discharging. *Nature* **2009**, *458*, 190.

(5) Guo, B.; Wang, X.; Fulvio, P. F.; Chi, M.; Mahurin, S. M.; Sun, X. G.; Dai, S. Soft-templated mesoporous carbon-carbon nanotube composites for high performance lithium-ion batteries. *Adv. Mater.* **2011**, *23*, 4661−4666.

(6) Bruce, P. G.; Scrosati, B.; Tarascon, J. M. Nanomaterials for rechargeable lithium batteries. *Angew. Chem., Int. Ed.* **2008**, *47*, 2930−2946.

(7) Qin, J.; Zhang, Q.; Cao, Z.; Li, X.; Hu, C.; Wei, B. MnO_x/SWCNT macro-films as flexible binder-free anodes for high-performance Li-ion batteries. *Nano Energy* **2013**, *2*, 733−741.

(8) Wang, X.; Fan, Y.; Susantyoko, R. A.; Xiao, Q.; Sun, L.; He, D.; Zhang, Q. High areal capacity Li ion battery anode based on thick mesoporous Co_3O_4 nanosheet networks. *Nano Energy* **2014**, *5*, 91−96.

(9) Wang, D.; He, H.; Han, L.; Lin, R.; Wang, J.; Wu, Z.; Liu, H.; Xin, H. L. Three-dimensional hollow-structured binary oxide particles as an advanced anode material for high-rate and long cycle life lithium-ion batteries. *Nano Energy* **2016**, *20*, 212−220.

(10) Chen, H.; Zhang, Q.; Wang, J.; Wang, Q.; Zhou, X.; Li, X.; Yang, Y.; Zhang, K. Mesoporous $ZnCo_2O_4$ microspheres composed of ultrathin nanosheets cross-linked with metallic $NiSi_x$ nanowires on Ni foam as anodes for lithium ion batteries. *Nano Energy* **2014**, *10*, 245−258.

DOI: 10.1021/acsomega.7b01228
ACS Omega 2017, 2, 7672−7681

(11) Poizot, P.; Laruelle, S.; Grugeon, S.; Dupont, L.; Tarascon, J. M. Nano-sized transition-metal oxides as negative-electrode materials for lithium-ion batteries. *Nature* **2000**, *407*, 496−499.
(12) Cao, X.; Wu, J.; Jin, C.; Tian, J.; Strasser, P.; Yang, R. $MnCo_2O_4$ anchored on P-doped hierarchical porous carbon as an electrocatalyst for high-performance rechargeable Li−O_2 batteries. *ACS Catal.* **2015**, *5*, 4890−4896.
(13) Li, J.; Xiong, S.; Li, X.; Qian, Y. A facile route to synthesize multiporous $MnCo_2O_4$ and $CoMn_2O_4$ spinel quasi-hollow spheres with improved lithium storage properties. *Nanoscale* **2013**, *5*, 2045−2054.
(14) Huang, G.; Xu, S.; Xu, Z.; Sun, H.; Li, L. Core−shell ellipsoidal $MnCo_2O_4$ anode with micro-/nano-structure and concentration gradient for lithium-ion batteries. *ACS Appl. Mater. Interfaces* **2014**, *6*, 21325−21334.
(15) Fu, C.; Li, G.; Luo, D.; Huang, X.; Zheng, J.; Li, L. One-step calcination-free synthesis of multicomponent spinel assembled microspheres for high-performance anodes of Li-ion batteries: a case study of $MnCo_2O_4$. *ACS Appl. Mater. Interfaces* **2014**, *6*, 2439−2449.
(16) Li, J.; Wang, J.; Liang, X.; Zhang, Z.; Liu, H.; Qian, Y.; Xiong, S. Hollow $MnCo_2O_4$ submicrospheres with multilevel interiors: from mesoporous spheres to yolk-in-double-shell structures. *ACS Appl. Mater. Interfaces* **2014**, *6*, 24−30.
(17) Chen, C.; Liu, B.; Ru, Q.; Ma, S.; An, B.; Hou, X.; Hu, S. Fabrication of cubic spinel $MnCo_2O_4$ nanoparticles embedded in graphene sheets with their improved lithium-ion and sodium-ion storage properties. *J. Power Sources* **2016**, *326*, 252−263.
(18) Wang, Y.; Wang, S.; Zhao, T.; Chen, Y.; Li, Z.; Wu, W.; Wu, M. Firmly combination of $CoMnO_x$ nanocrystals supported on N-doped CNT for lithium-ion batteries. *Chem. Eng. J.* **2016**, *306*, 336−343.
(19) Yun, Y. J.; Kim, J. K.; Ju, J. Y.; Unithrattil, S.; Lee, S. S.; Kang, Y.; Jung, H. K.; Park, J. S.; Im, W. B.; Choi, S. A morphology, porosity and surface conductive layer optimized $MnCo_2O_4$ microsphere for compatible superior Li^+ ion/air rechargeable battery electrode materials. *Dalton Trans.* **2016**, *45*, 5064−5070.
(20) Kraytsberg, A.; Ein-Eli, Y. Conveying Advanced Li ion Battery Materials into Practice the Impact of Electrode Slurry Preparation Skills. *Adv. Energy Mater.* **2016**, *6*, No. 1600655.
(21) Bhattacharjya, D.; Sinhamahapatra, A.; Ko, J. J.; Yu, J.-S. High capacity and exceptional cycling stability of ternary metal sulfide nanorods as Li ion battery anodes. *Chem. Commun.* **2015**, *51*, 13350−13353.
(22) Li, L.; Zhang, Y. Q.; Liu, X. Y.; Shi, S. J.; Zhao, X. Y.; Zhang, H.; Ge, X.; Cai, G. F.; Gu, C. D.; Wang, X. L.; Tu, J. P. One-dimension $MnCo_2O_4$ nanowire arrays for electrochemical energy storage. *Electrochim. Acta* **2014**, *116*, 467−474.
(23) Hou, X.; Wang, X.; Liu, B.; Wang, Q.; Luo, T.; Chen, D.; Shen, G. Hierarchical MnCo2O4 nanosheet arrays/carbon cloths as integrated anodes for lithium-ion batteries with improved performance. *Nanoscale* **2014**, *6*, 8858−8864.
(24) Wei, Q.; An, Q.; Chen, D.; Mai, L.; Chen, S.; Zhao, Y.; Hercule, K. M.; Xu, L.; Khan, M.; Zhang, Q. One-pot synthesized bicontinuous hierarchical $Li_3V_2(PO_4)_3$/C mesoporous nanowires for high-rate and ultralong-life lithium-ion batteries. *Nano Lett.* **2014**, *14*, 1042−1048.
(25) Chen, L.; Yan, B.; Xu, J.; Wang, C.; Chao, Y.; Jiang, X.; Yang, G. Bicontinuous structure of Li3V2 (PO4) 3 clustered via carbon nanofiber as high-performance cathode material of Li-ion batteries. *ACS Appl. Mater. Interfaces* **2015**, *7*, 13934−13943.
(26) Wang, T.; Shi, S.; Li, Y.; Zhao, M.; Chang, X.; Wu, D.; Wang, H.; Peng, L.; Wang, P.; Yang, G. Study of microstructure change of carbon nanofibers as binder-free anode for high-performance lithium-ion batteries. *ACS Appl. Mater. Interfaces* **2016**, *8*, 33091−33101.
(27) Wang, T.; Li, H.; Shi, S.; Liu, T.; Yang, G.; Chao, Y.; Yin, F. 2D film of carbon nanofibers elastically astricted MnO microparticles: a flexible binder-free anode for highly reversible lithium ion storage. *Small* **2017**, *13*, No. 1604182.
(28) Zhao, M.; Liu, Y.; Jiang, J.; Ma, C.; Yang, G.; Yin, F.; Yang, Y. Sheath/core hybrid $FeCO_3$/carbon nanofibers as anode materials for superior cycling stability and rate performance. *ChemElectroChem* **2017**, *4*, 1450.
(29) Yang, G.; Li, Y.; Ji, H.; Wang, H.; Gao, P.; Wang, L.; Liu, H.; Pinto, J.; Jiang, X. Influence of Mn content on the morphology and improved electrochemical properties of Mn3O4| MnO@ carbon nanofiber as anode material for lithium batteries. *J. Power Sources* **2012**, *216*, 353−362.
(30) Yang, D.-S.; Chaudhari, S.; Rajesh, K. P.; Yu, J.-S. Preparation of Nitrogen-Doped Porous Carbon Nanofibers and the Effect of Porosity, Electrical Conductivity, and Nitrogen Content on Their Oxygen Reduction Performance. *ChemCatChem* **2014**, *6*, 1236−1244.
(31) Tan, B. J.; Klabunde, K. J.; Sherwood, P. M. XPS studies of solvated metal atom dispersed (SMAD) catalysts. Evidence for layered cobalt-manganese particles on alumina and silica. *J. Am. Chem. Soc.* **1991**, *113*, 855−861.
(32) Needham, S. A.; Wang, G. X.; Konstantinov, K.; Tournayre, Y.; Lao, Z.; Liu, H. K. Electrochemical Performance of Co_3O_4-C Composite Anode Material. *Electrochem. Solid-State Lett.* **2006**, *9*, A315−A319.
(33) Yuvaraj, S.; Vignesh, A.; Shanmugam, S.; Selvan, R. K. Nitrogen-Doped Multi-Walled Carbon Nanotubes-$MnCo_2O_4$ Microsphere as Electrocatalyst for Efficient Oxygen Reduction Reaction. *Int. J. Hydrogen Energy* **2016**, *41*, 15199−15207.
(34) Ma, Y.; Tai, C. W.; Younesi, R.; Gustafsson, T.; Lee, J. Y.; Edström, K. Iron doping in spinel NiMn2O4: stabilization of the mesoporous cubic phase and kinetics activation toward highly reversible Li^+ storage. *Chem. Mater.* **2015**, *27*, 7698−7709.
(35) Liu, B.; Hu, X.; Xu, H.; Luo, W.; Sun, Y.; Huang, Y. Encapsulation of MnO nanocrystals in electrospun carbon nanofibers as high-performance anode materials for lithium-ion batteries. *Sci. Rep.* **2014**, *4*, No. 4229.
(36) Su, J.; Liang, H.; Gong, X. N.; Ly, X. Y.; Long, Y. F.; Wen, Y. X. Fast Preparation of Porous MnO/C Microspheres as Anode Materials for Lithium-ion Batteries. *Nanomaterials* **2017**, *7*, 121.
(37) Zheng, F.; Yang, Y.; Chen, Q. High lithium anodic performance of highly nitrogen-doped porous carbon prepared from a metal-organic framework. *Nat. Commun.* **2014**, *5*, No. 5261.
(38) Wu, Y.; Reddy, M. V.; Chowdari, B. V. R.; Ramakrishna, S. Long-term cycling studies on electrospun carbon nanofibers as anode material for lithium ion batteries. *ACS Appl. Mater. Interfaces* **2013**, *5*, 12175−12184.
(39) Bard, A.; Faulkner, L. *Electrochemical Methods. Fundamentals and Applications*, 2nd ed.; John Wiley and Sons Inc.: New York, 2001; pp 156−225.
(40) Wang, K.; Zhao, C.; Min, S.; Qian, X. Facile synthesis of Cu_2O/RGO/$Ni(OH)_2$ nanocomposite and its double synergistic effect on supercapacitor performance. *Electrochim. Acta* **2015**, *165*, 314−322.
(41) Shaju, K. M.; Jiao, F.; Débart, A.; Bruce, P. G. Mesoporous and nanowire Co_3O_4 as negative electrodes for rechargeable lithium batteries. *Phys. Chem. Chem. Phys.* **2007**, *9*, 1837−1842.
(42) Kim, M.-S.; Bhattacharjya, D.; Fang, B.; Yang, D.-S.; Bae, T.-S.; Yu, J.-S. Morphology-dependent Li storage performance of ordered mesoporous carbon as anode material. *Langmuir* **2013**, *29*, 6754−6761.
(43) Chen, R.; Hu, Y.; Shen, Z.; Chen, Y.; He, X.; Zhang, X.; Zhang, Y. Controlled Synthesis of Carbon Nanofibers Anchored with $Zn_xCo_{3-x}O_4$ Nanocubes as Binder-Free Anode Materials for Lithium-Ion Batteries. *ACS Appl. Mater. Interfaces* **2016**, *8*, 2591−2599.
(44) Zhang, C.; Yu, J.-S. Morphology-tuned synthesis of $NiCo_2O_4$-coated 3D graphene architectures used as binder-free electrodes for lithium ion batteries. *Chem. − Eur. J.* **2016**, *22*, 4422−4430.
(45) Chaudhari, S.; Bhattacharjya, D.; Yu, J.-S. Facile synthesis of hexagonal $NiCo_2O_4$ nanoplates as high performance anode material for lithium ion batteries. *Bull. Korean Chem. Soc.* **2015**, *36*, 2330−2336.

DOI: 10.1021/acsomega.7b01228
ACS Omega 2017, 2, 7672−7681